DTU Library

Visualizing thickness-dependent magnetic textures in few-layer Cr$_2$Ge$_2$Te$_6$

Vervelaki, Andriani; Bagani, Kousik; Jetter, Daniel; Doan, Manh Ha; Chau, Tuan K.; Gross, Boris; Christensen, Dennis V.; Bøggild, Peter; Poggio, Martino

Visualizing thickness-dependent magnetic textures in few-layer $Cr_2Ge_2Te_6$

Check for updates

Andriani Vervelaki[1], Kousik Bagani[1], Daniel Jetter[1], Manh-Ha Doan[2], Tuan K. Chau[2], Boris Gross[1], Dennis V. Christensen [3], Peter Bøggild [2] & Martino Poggio [1,4] ✉

Magnetic ordering in two-dimensional (2D) materials has recently emerged as a promising platform for data storage, computing, and sensing. To advance these developments, it is vital to gain a detailed understanding of how the magnetic order evolves on the nanometer-scale as a function of the number of atomic layers and applied magnetic field. Here, we image few-layer $Cr_2Ge_2Te_6$ using a combined scanning superconducting quantum interference device and atomic force microscopy probe. Maps of the material's stray magnetic field as a function of applied magnetic field reveal its magnetization per layer as well as the thickness-dependent magnetic texture. Using a micromagnetic model, we correlate measured stray-field patterns with the underlying magnetization configurations, including labyrinth domains and skyrmionic bubbles. Comparison between real-space images and simulations demonstrates that the layer dependence of the material's magnetic texture is a result of the thickness-dependent balance between crystalline and shape anisotropy. These findings represent an important step towards 2D spintronic devices with engineered spin configurations and controlled dependence on external magnetic fields.

The recent discovery of long-range ferromagnetic ordering in bilayer $Cr_2Ge_2Te_6$ (CGT) and monolayer CrI_3 has opened the fascinating new area of two-dimensional (2D) magnetic materials[1–3]. These materials often have different magnetic properties from those of their bulk counterparts and these properties can be strongly dependent on the number of layers. For instance, although bulk CrI_3 is ferromagnetic, it is antiferromagnetic in the few-layer limit[4–6]. Furthermore, the inter-layer exchange interaction can lead to antiferromagnetic or ferromagnetic behavior depending on whether the layers are stacked in a monoclinic or rhombohedral manner[7–9]. Indeed, the possibility of engineering van der Waals (vdW) heterostructures from these systems—atomic layer by atomic layer—affords unprecedented control over their magnetism. Moreover, unlike bulk magnets, 2D magnets are highly susceptible to external stimuli, including electric fields, magnetic fields, and strain[10]. For all of these reasons, 2D magnets have potential applications ranging from high-density data storage and efficient information processing to sensing.

Among these materials, the ferromagnetic semiconductor CGT is especially promising for spintronic and memory storage applications. Both current[11] and laser[12] induced magnetization switching has been demonstrated in this material. It exhibits spin-orbit torque switching under very low current densities, making it promising for low-power memory devices[13].

In addition, CGT is a candidate for pressure-sensitive spintronic applications, because of its strong anisotropic spin-lattice coupling[14]. Although CGT has a low Curie temperature $T_c = 68$ K in the bulk, which drops to 30 K in the bilayer limit[1], several methods have succeeded at increasing T_c, including via doping[15,16] and strain[17,18]. In particular, the application of 2.3% strain has been shown to raise T_c up to room temperature.

Because of these promising properties, its magnetic behavior and—specifically—the dependence of this behavior on the number of layers needs to be understood. Since the first magnetic imaging of CGT, studies have been carried out on samples of different thicknesses[19–23]. Few-layer CGT with thicknesses between 2 and 5 nm shows soft ferromagnetic behavior with an out-of-plane magnetic easy-axis and no magnetic domains[1]. In contrast, hysteretic behavior with multi-domain magnetic textures is observed in CGT flakes with thicknesses in the tens of nanometers[19–21]. For samples thicker than about 100 nm, the presence of Bloch-type magnetic stripe domains and skyrmionic bubbles has been reported[23]. Despite these observations, the evolution of magnetic order with thickness, i.e., the transition from single-domain soft ferromagnetic behavior in few-layers to multi-domain structure in the thicker limit has not been investigated. Also, the type of magnetization textures forming the domains observed in the intermediate thickness range remains unclear.

[1]Department of Physics, University of Basel, 4056 Basel, Switzerland. [2]Department of Physics, Technical University of Denmark, 2800 Kongens Lyngby, Denmark. [3]Department of Energy Conversion and Storage, Technical University of Denmark, 2800 Kongens Lyngby, Denmark. [4]Swiss Nanoscience Institute, University of Basel, 4056 Basel, Switzerland. ✉e-mail: martino.poggio@unibas.ch

In this work, we investigate the dependence of CGT's magnetic behavior on thickness down to the few-layer limit. We image the material's stray magnetic field, determine the corresponding magnetization configuration, and map its evolution as a function of applied magnetic field. Nanometer-scale magnetic imaging is carried out via a superconducting quantum interference device (SQUID) integrated on a cantilever scanning probe at 4.2 K[24]. The SQUID-on-lever's (SOL) ability to simultaneously image both the sample's topography and stray field allows us to correlate material thickness with magnetic configuration. Furthermore, a comparison of the measured stray-field maps with micromagnetic simulations sheds light on the form of the underlying magnetization configurations and the magnetic interactions which produce them.

Results and discussion
Magnetization per layer
CGT flakes are mechanically exfoliated on a Si/SiO$_2$ substrate. Because CGT is prone to degrade in ambient conditions[1], flakes are covered with 10-nm-thick hexagonal boron nitride (hBN) immediately after exfoliation. Figure 1a shows an optical image of a flake with regions of various thicknesses. These regions can be distinguished by their different optical contrast. Their thickness is measured via atomic force microscopy (AFM) (see Supplementary Note 1 and Supplementary Fig. 1), acquired by the SOL scanning probe in non-contact mode. In Fig. 1b, AFM cross-sections taken across the boundaries between regions of different thicknesses show steps in integer multiples of 0.7 nm, which is the thickness of a single atomic layer. The number of

layers in each region is then determined using this thickness per layer and a thickness of 1.1 nm for the first layer[1]. The estimated thickness of the flake ranges from 2 to 16 layers with integer layer steps between adjacent areas. The availability of different thicknesses on the same flake allows us to study the evolution of its magnetic behavior as a function of the number of layers.

The magnetic properties of a CGT flake are investigated by imaging the out-of-plane component of the sample's magnetic stray field, $B_z(x, y)$, in a plane above the sample. Initially, we apply an out-of-plane magnetic field $\mu_0 H_z = -133$ mT in order to saturate the magnetization of the flake. The resulting $B_z(x, y)$, shown in Fig. 1c, is peaked at the edges of the flake or at boundaries between regions of different thicknesses, as expected for a sample uniformly magnetized in the out-of-plane direction. The thinnest regions on the bottom-left corner of the image (indicated with black and yellow dots) are 2 and 3 layers thick and show very weak magnetic signatures, visible in $\frac{dB_z(x,y)}{dx}$, shown in Fig. 1d.

From $B_z(x, y)$, shown in Fig. 1c, we then determine the sample's out-of-plane magnetization $M_z(x, y)$, shown in Fig. 1e. By assuming that the magnetization is fully saturated along the z-direction and confined to a 2D plane (the sample is much thinner than the probe-sample distance), we use a reverse propagation method to solve for $\mathbf{M} = \mathbb{A}^{-1}\mathbf{B}$ where $\mathbb{A}$ is the transfer matrix[25]. Figure 1f shows the reconstructed magnetization averaged over areas of uniform thickness, M_z^{avg}, as a function of the number of layers. In particular, the magnetization of each area increases linearly with the number of layers. From the slope of the linear fit, we obtain a magnetization per layer $M_z^{\mathrm{layer}} = (10.9 \pm 0.8)\,\mu_B\,\mathrm{nm}^{-2}$, equivalent to a saturation magnetization
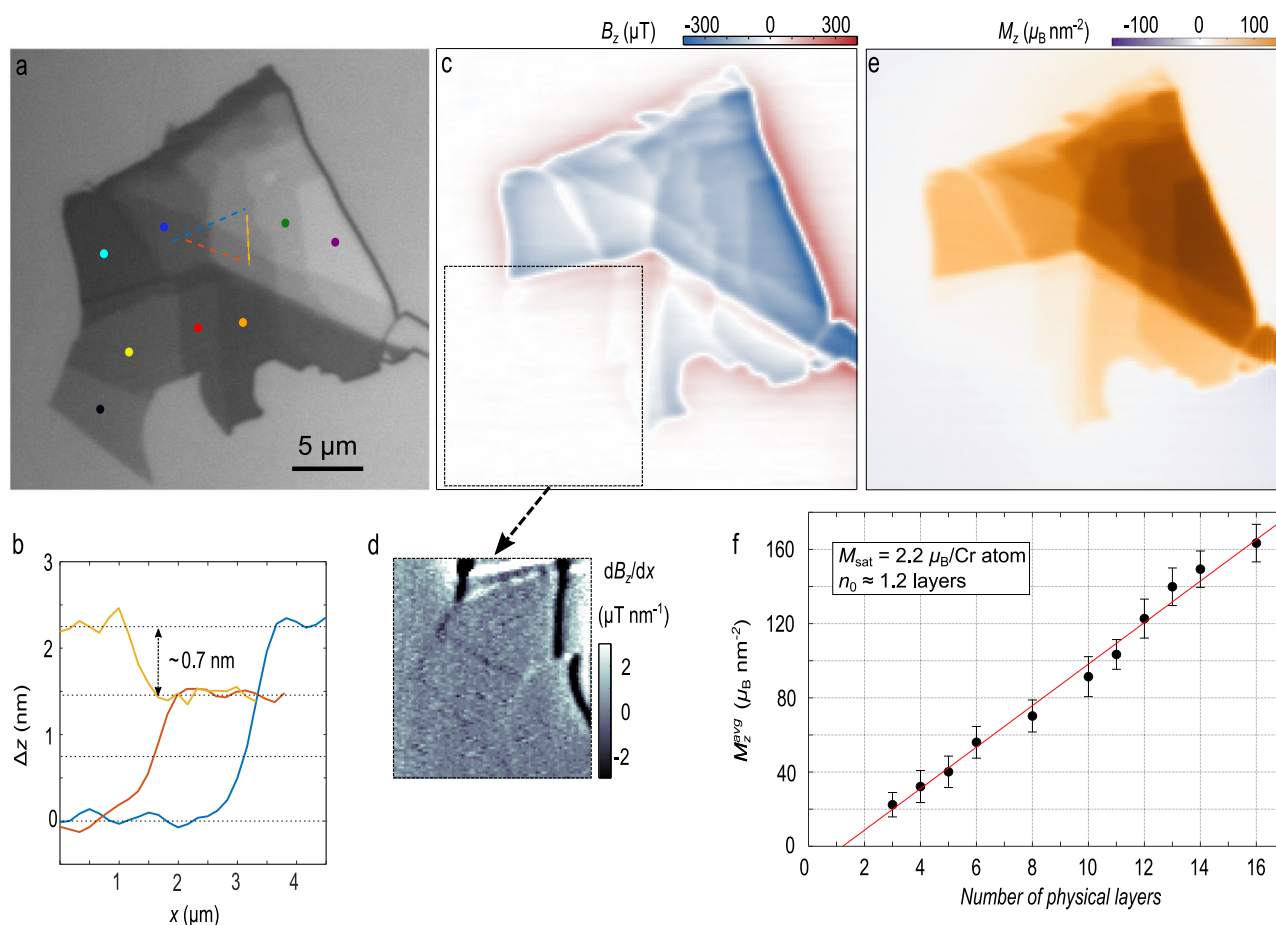

Fig. 1 | Magnetization per layer. a Optical image of the CGT flake. Regions of different thickness can be identified from the optical contrast and are indicated with black, yellow, red, orange, aquamarine, blue, green, and purple circles for thicknesses of 2, 3, 4, 6, 8, 10, 14, and 16 layers, respectively. **b** AFM scans between regions of uniform thickness showing steps of integer layer thickness along the correspondingly colored dashed lines in (**a**). **c** Out-of-plane component of the stray

magnetic field $B_z(x, y)$ measured above the sample in an applied out-of-plane field, $\mu_0 H_z = -133$ mT. **d** Numerical derivative along the x-axis, $\frac{dB_z(x,y)}{dx}$ of the region indicated by the black dotted square in (**c**). **e** Out-of-plane magnetization $M_z(x, y)$ calculated from (**c**). **f** M_z^{avg} plotted as a function of the number of layers and its corresponding linear fit shown with the red line.

$M_{\text{sat}} = (2.2 \pm 0.2)\,\mu_B/\text{Cr}$ atom, which is consistent with previous reports[26–28]. From the non-zero horizontal intercept of the fit, we find that the flake contains $n_0 = 1.2 \pm 0.6$ magnetically inactive layers. This effect is likely due to the degradation of the outer surfaces of the flake during the short exposure to air before encapsulation. Hereafter, the number of layers of CGT refers to the number of magnetically active layers, which are roughly one less than the number of physical layers. By considering the geometry of the sample and the number of magnetically active layers in each region, we calculate $B_z(x, y)$ for a saturated flake with $M_{\text{sat}} = 2.2\,\mu_B/\text{Cr}$. As discussed in Supplementary Note 4 and shown in Supplementary Fig. 6, this calculation matches the measured $B_z(x, y)$ of Fig. 1c.

Thickness-dependent magnetic hysteresis

To investigate the process of magnetic reversal and its dependence on thickness, we map $B_z(x, y)$ as a function of applied magnetic field. Figure 2a–i shows the evolution of the flake's magnetization reversal with respect to out-of-plane applied field H_z. Starting in the saturated state, initialized at $\mu_0 H_z = -133$ mT, the applied field is gradually stepped toward zero, into reverse field, and past saturation to 140 mT. Until zero applied field, the magnetization in the thicker regions (10–15 layers) remains almost unchanged, whereas, in the thinner parts of the flake (5–7 layers), domains start to form around $\mu_0 H_z = -10$ mT (more apparent in Supplementary Fig. 4, discussed in Supplementary Note 3). Upon reversing the direction of H_z, magnetic domains also nucleate in the thicker regions of the flake. With increasing reverse field H_z, these domains spread over the whole flake and result in a complete reversal of the magnetization by $\mu_0 H_z \sim 40$ mT. Inverting this procedure results in a symmetric reversal process (see Supplementary Figs. 3 and 4).

Figure 2j shows $B_z(x, y)$ averaged over two different areas of constant thickness, B_z^{avg}, as a function of H_z. These local hysteresis loops are shown for the 7 and 15-layer-thick regions indicated in Fig. 2a, though a full set can be found in Supplementary Fig. 5, which is discussed in Supplementary Note 3. Thinner regions of the sample with 7 layers or less, do not show measurable magnetic remanence within the detection limit and have magnetization curves characteristic of a soft ferromagnet. This behavior is consistent with previous observations in 6-layer flakes (2% magnetic remanence), although the measured saturation field of ~40 mT is significantly smaller than the previously reported value of ~0.6 T[1]. In contrast, regions of the sample thicker than about 9 layers show finite coercivity with a magnetic remanence of 70–80% of the saturation magnetization M_{sat}. This behavior transforms for increasing thickness into bow-tie-shaped hysteresis for 13 layers or more as exemplified by the data shown for the 15-layer-thick region. Noah et al.[19] also reported an open hysteresis loop with 100% magnetic remanence for thicknesses less than 10 nm (14 layers) and a bow-tie hysteresis with no magnetic remanence for thicknesses more than 15 nm (21 layers). Bow-tie-shaped hysteresis is a sign of percolating magnetic domains, magnetic vortices, or skyrmion formation during magnetic reversal[29–32]. Our measurements give a complete picture of the gradual transition of the magnetic hysteresis loop from soft ferromagnetic to bow-tie shape with increasing thickness, pointing to an evolution of the corresponding magnetic textures with thickness (see Supplementary Fig. 5, discussed in Supplementary Note 3).

Layer-dependent magnetization texture

Our local magnetic measurements confirm that magnetic reversal in few-layer CGT depends on thickness. In order to shed light on the magnetization configurations corresponding to measured stray field patterns, we turn to micromagnetic simulations. We use a model based on the Landau-Liftshitz-Gilbert formalism, which is based on the geometry of the flake and known material parameters (see "Methods" for details). We focus on three areas of the flake representing the behavior observed in the thick (13–15 layers), intermediate (7–9 layers), and thin regions (3–5 layers) of the sample. In our model, we use one less layer compared to the actual number of physical layers in the flake, based on our measurement of approximately one magnetically inactive layer. In Fig. 3a–i, we show

$B_z^{\text{lever}}(x, y)$ measured above the sample with applied out-of-plane field $\mu_0 H_z = 7.5$ mT along with corresponding simulations of $\frac{dB_z(x,y)}{dz}$ and $M_z(x, y)$. $B_z^{\text{lever}}(x, y) \propto \frac{dB_z(x,y)}{dz}$ and is measured by oscillating the cantilever on resonance and demodulating the SQUID-on-lever response at this frequency (see "Methods"). It provides a more sensitive measure of small spatial features than $B_z(x, y)$.

Measured $B_z^{\text{lever}}(x, y)$ maps of all three regions agree well with the simulated $\frac{dB_z(x,y)}{dz}$, which reproduce the shapes, relative amplitudes, and characteristic lengths of the observed patterns. Furthermore, simulated magnetic hysteresis curves, shown in Fig. 3j, for the 7 and 15-layer-thick regions reproduce local hysteresis measurements shown in Fig. 2j. Given this agreement, we can turn to the corresponding simulated $M_z(x, y)$ configurations as the likely magnetization textures present in those regions of the sample.

In particular, simulations of the thick region (13–15 layers), which is indicated by the green and purple dots in Fig. 1a, point to the presence of labyrinth domains, as shown in Fig. 3c. These structures are responsible for the bow-tie hysteresis behavior, which we observe in CGT flakes thicker than 13 layers, shown in Fig. 2j. A closer look at the simulations reveals that the labyrinth domains are separated by Néel-type domain walls in both surface layers, which gradually transform toward Bloch-type domain walls in the interior layers (see Supplementary Fig. 10 and Supplementary Note 5). Simulated $M_z(x, y)$ for the intermediate region with 7 to 9 layers, as indicated by the aquamarine dot in Fig. 1a, reveals long stripe domains (Fig. 3f). Simulated $M_z(x, y)$ for the thin region with 3 to 5 layers also shows stripe domains for 5 layers, but no domains for 3 layers. The absence of domains, in combination with soft ferromagnetic behavior in the very thin limit, is consistent with a previous report by Gong et al.[1]. The measured and simulated evolution of magnetic domains as a function of increasing applied field is compared in Supplementary Figs. 7–9 and discussed in Supplementary Note 5.

In our simulations, the presence of labyrinth domains in thick CGT as well as their transition to stripes, and—eventually—to regions without domains as thickness is reduced is robust to small adjustments of the material parameters and sample geometry. In fact, the strong layer dependence of the magnetization configuration is a direct result of the similar magnitudes of magnetocrystalline and shape anisotropy in the few-layer samples. As the thickness of the sample changes, the balance between magnetocrystalline anisotropy, which favors out-of-plane magnetization alignment, and shape anisotropy, which favors in-plane alignment, is altered. The fact that this model reproduces the measured layer dependence suggests that the same mechanisms are at work in the experiment.

However, in order to optimally match both simulated hysteresis curves and magnetic images with the corresponding measurements, both the magnetocrystalline anisotropy K_u and the in-plane exchange stiffness A_{ex} must be reduced when simulating the thinner parts of the flake compared to the thicker parts (see "Methods"). The need to tune these parameters to achieve the best agreement suggests a dependence of A_{ex} and K_u on thickness. Although the mechanisms for such an effect remain unclear, a dependence of exchange interactions, and consequently A_{ex}, on the layer number has been predicted theoretically[33]. Another indication for such dependence is provided by the observation of a rapid drop in T_c as a function of decreasing thickness in CGT[1].

Skyrmionic magnetization texture

Simulations of the thick part of the sample (12 to 15 layers thick) reveal labyrinth domains with similar magnetization patterns as were previously observed in flakes in the range of 100 nm or thicker[23]. In those experiments, it was observed that under increasing H_z, the labyrinth domains transform into bubbles that are mostly homochiral. Such bubbles are topologically identical to skyrmions and are characterized by a topological charge of ± 1. Topologically non-trivial spin textures like skyrmions are usually stabilized in non-centrosymmetric magnetic systems via a Dzyaloshinskii-Moriya interaction (DMI)[34], which is not present in this system. Nevertheless, the competition between uniaxial anisotropy and magnetostatic energy can give
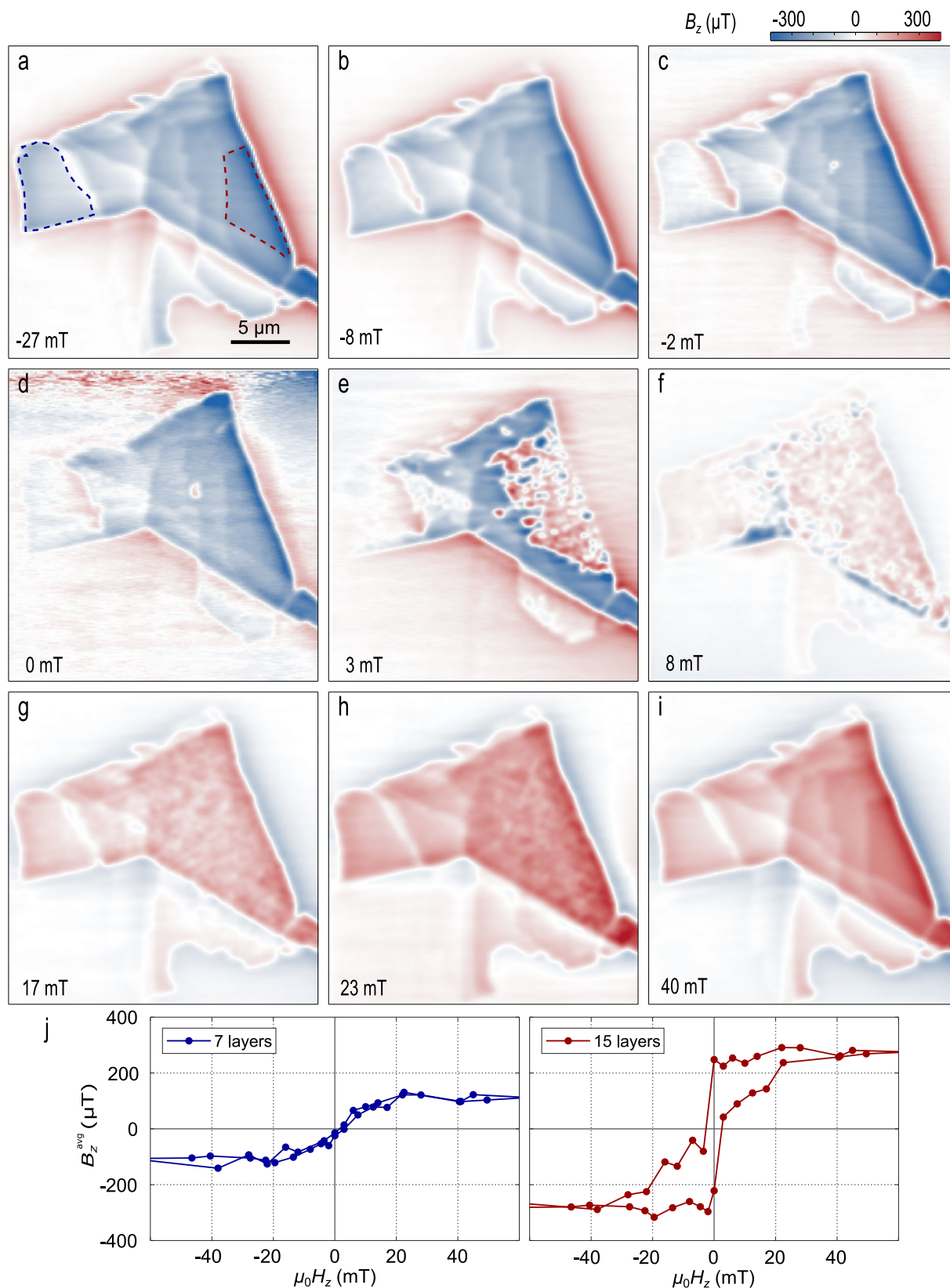
Fig. 2 | Visualizing the out-of-plane magnetic hysteresis. a–i $B_z(x, y)$ measured above the sample at different $\mu_0 H_z$ as indicated by the value shown in each image. $\mu_0 H_z$ is slowly stepped from -133 mT to 140 mT. Blue and red dashed lines highlight the 7 and 15-layer-thick regions of the flake. Images for more values of $\mu_0 H_z$ can be found in Supplementary Fig. 3, which is discussed in Supplementary Note 3. **j** B_z^{avg} for areas of constant thickness highlighted in (**a**) plotted against $\mu_0 H_z$.
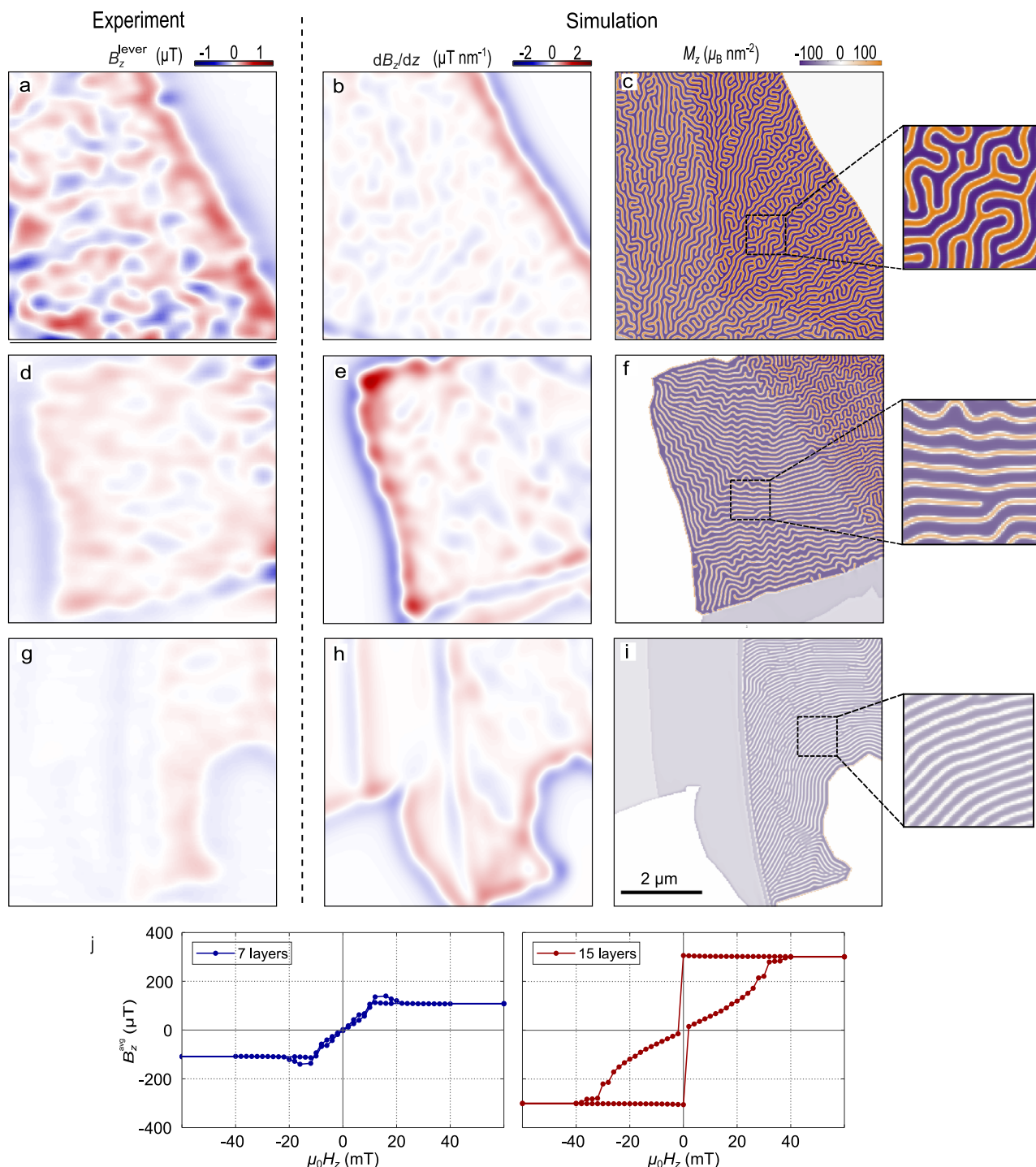
Fig. 3 | Evolution of magnetic domains with thickness. a $B_z^{lever}(x, y)$ measured at $\mu_0 H_z = 7.5$ mT over the 13 to 15-layer-thick region of the sample indicated by green and purple dots in Fig. 1a, together with the corresponding simulation of (**b**) $\frac{dB_z(x,y)}{dz}$ and (**c**) $M_z(x, y)$. **d–f** A similar measurement at the same H_z over the 7 to 9-layer-thick region of the sample, indicated by the aquamarine dot in Fig. 1a, together with corresponding simulations. **g–i** A final measurement at the same H_z over the 3 to 5-layer-thick region indicated by the red and orange dots in Fig. 1a, together with corresponding simulations. **j** Simulated local hysteresis for 7 and 15 layers.

rise to a plethora of magnetic patterns including labyrinth domains, stripes, and skyrmionic bubbles[35,36].

To determine whether such skyrmionic bubbles are found in few-layer-thick CGT, we field-cool the sample at $\mu_0 H_z = 10$ mT. Figure 4a shows a measurement of $B_z^{lever}(x, y)$ over the thick part of the field-cooled sample after the applied field was increased to $\mu_0 H_z = 17$ mT. Stray field patterns characteristic of labyrinth domains are visible over most of the 15-layer-thick region with some percolating features expanding to neighboring regions. As shown in Fig. 4b, after the field is further increased to

$\mu_0 H_z = 28$ mT, the patterns related to labyrinth domains shrink and transform into bubble-like features.

In corresponding micromagnetic simulations, we mimic the field-cooling procedure by starting with an arbitrary labyrinth domain, applying $\mu_0 H_z = 10$ mT, and then letting the system relax to find the minimum energy state. The resulting simulated $\frac{dB_z(x,y)}{dz}$ and $M_z(x, y)$ in Fig. 4c, e, simulated at $\mu_0 H_z = 26$ mT, present features similar to those measured in the field-cooled $B_z^{lever}(x, y)$. The corresponding $M_z(x, y)$ shows that stripe domains start from the edge of the flake, form multiple branches, and expand to the
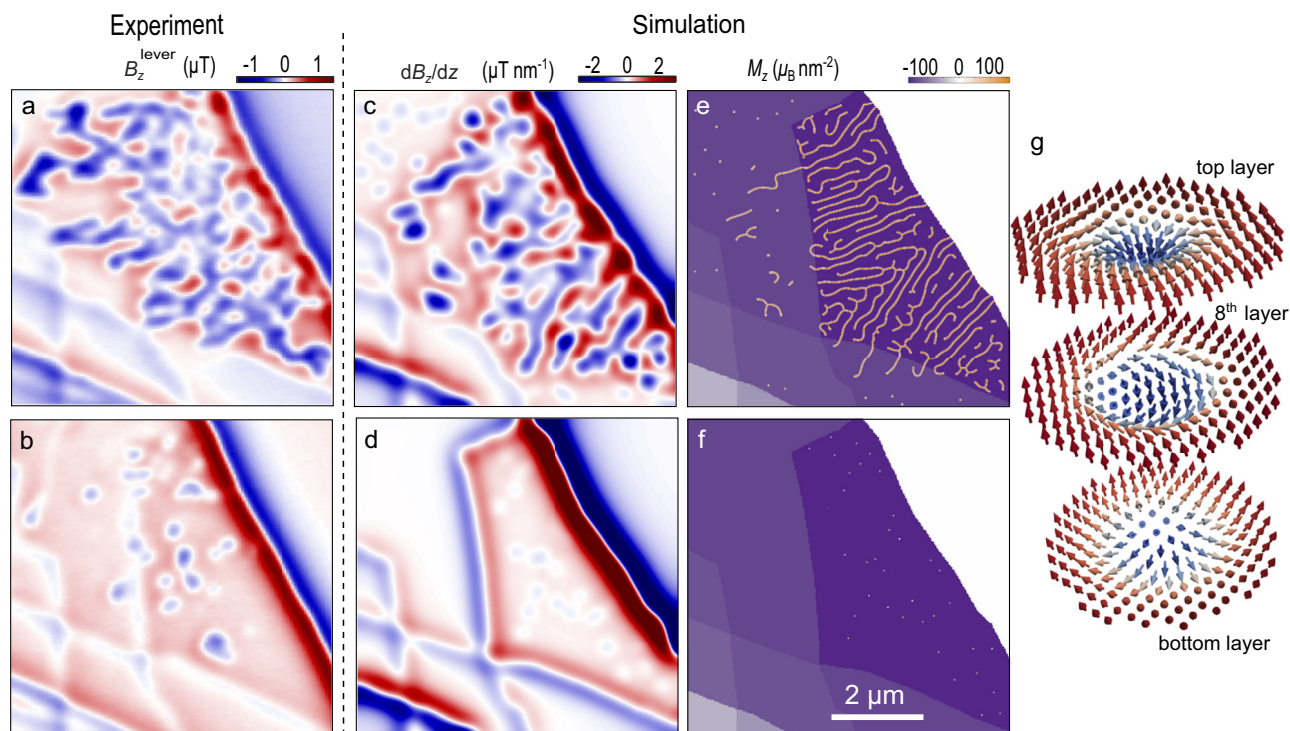
Fig. 4 | Skyrmionic spin texture. a, b $B_z^{lever}(x, y)$ maps of the thick part of the sample at $\mu_0 H_z = 17$ mT and 28 mT, respectively, after field-cooling in 10 mT. **c–f** Corresponding $\frac{dB_z(x,y)}{dz}$ and magnetization $M_z(x,y)$ simulated at $\mu_0 H_z = 26$ mT and 38 mT, respectively, showing stripe domains shrink into bubbles at higher field.

g The simulated magnetization configuration of the magnetic bubbles at $\mu_0 H_z = 38$ mT, showing a Bloch-type skyrmionic texture in the middle layer, which gradually transforms into a Néel-type texture at the surface layers.

thinner regions. These domains are very similar to the domains shown in Fig. 3a–c. As the field is increased in the simulations to $\mu_0 H_z = 38$ mT, the corresponding $\frac{dB_z(x,y)}{dz}$ map in Fig. 4d qualitatively matches the bubble-like features in the measured $B_z^{lever}(x, y)$. $M_z(x, y)$ maps reveal that, upon the increase of H_z, the underlying domains shrink and transform into bubbles, most of which have skyrmionic magnetization texture, as shown in Fig. 4f. Based on the excellent agreement between experiment and simulation, we can conclude the most probable spin texture behind the bubble-like features shown in Fig. 4b to be skyrmionic bubbles. As was observed in our magnetization simulations of the labyrinth domains, whose helicity transforms through the thickness of the flake, the skyrmionic bubbles also show a modulating helicity from the top to the bottom layer, as schematically shown in Fig. 4g. This behavior has been previously proposed in systems with skyrmions[37] and has also been observed in skyrmionic bubbles[38]. Such bubbles can also be obtained by zero-field-cooling this sample (see Supplementary Fig. 4).

Conclusion

We have investigated the thickness dependence of magnetic ordering in CGT down to the few-layer limit. The measured magnetic hysteresis for different numbers of layers reveals a transition from a bow-tie hysteretic behavior to a soft behavior without remanence for less than 8 layers. Comparison with micromagnetic simulations indicates that complex stray field patterns observed for CGT thicker than 5 layers result from labyrinth and stripe-like magnetization configurations and—under some conditions—from skyrmionic bubbles. These complex magnetic textures emerge from the competition between magnetocrystalline anisotropy and magnetostatic interactions. Our experimental results are reproduced by micromagnetic simulations under the assumption that the magnitude of these two energies is similar. The agreement is further optimized in the thinnest regions of the sample assuming a decreasing magnetocrystalline anisotropy and exchange stiffness with the decreasing number of layers. Although the mechanism for this dependence of the material's magnetic properties is unclear, the

decrease in exchange stiffness with decreasing number of layers has been suggested theoretically[33]. Nevertheless, we cannot exclude that external factors, which could also vary as a function of sample thickness, including level of oxidation or defect density, could be responsible.

Methods

Cr₂Ge₂Te₆/hBN heterostructure fabrication

The heterostructure is fabricated in ambient conditions using a dry viscoelastic stamping method[39]. CGT flakes with different thicknesses are first mechanically exfoliated from a single crystal (HQ graphene) onto a SiO₂/Si substrate with pre-patterned number markers. A 10-nm-thick hBN flake is exfoliated from the bulk form on the Polydimethylsiloxane (PDMS) thin film and then stacked on top of the CGT flake for passivation. To minimize degradation of the CGT surface, the stacking process is carried out below 120 °C in all steps and handled within less than 10 min[20].

SQUID-on-lever

We pattern a nanometer-scale SQUID via focused-ion-beam (FIB) milling at the apex of a cantilever coated with Nb[24]. The top side of the cantilever is deposited with 50 nm of Nb and 20 nm of Au to create a superconducting film with enhanced resistance against ion implantation effects of subsequent Ga⁺-FIB milling steps. Before film deposition, FIB milling is used to create a 650-nm-wide plateau on the cantilever's tip. After film deposition, FIB milling is used to separate two superconducting leads across the cantilever and to create a superconducting loop with a diameter of 80 nm with two constriction-type Josephson junctions on the plateau. The SQUID is characterized and operated at 4.2 K in a semi-voltage biased circuit and its current I_{SQ} is measured by a series SQUID array amplifier (Magnicon). The effective diameter of the SQUID extracted from the interference pattern (see Supplementary Fig. 2 and Supplementary Note 2) is 270 nm. The SQUID attains a DC magnetic flux sensitivity of $S_\phi = 1 \, \mu\Phi_0 \, \text{Hz}^{-1/2}$ and an AC flux sensitivity at 10 kHz of $S_\phi = 0.2 \, \mu\Phi_0 \, \text{Hz}^{-1/2}$ and remains sensitive up to $\mu_0 H_z > 250$ mT (see Supplementary Fig. 2).

Hybrid imaging

The SOL scanning probe is capable of simultaneously performing AFM and scanning SQUID microscopy (SSM). It operates in a custom-built scanning setup under high vacuum in a ^{4}He cryostat. Non-contact AFM is carried out using a fiber-optic interferometer to measure the cantilever displacement and a piezo-electric actuator driven by a phase-locked loop (PLL) to resonantly excite the cantilever at $f_0 = 285.28$ kHz to an amplitude $\Delta z = 16$ nm.

Since the current response of the SQUID-on-lever is proportional to the magnetic flux threading through it, this response provides a measure of the z-component of the local magnetic field integrated over the loop. We measure a calibration curve (I_{SQ} vs. $\mu_0 H_z$) before and after each scan, ensuring that the SQUID response is linear for a field range larger than that produced by the flake. Because of the asymmetry in the SQUID, the response is non-zero and monotonic even at $\mu_0 H_z = 0$ mT, although the response is weaker than at other fields and must be calibrated by fitting with a higher order polynomial. By scanning the sample using piezo-electric actuators at a constant tip-sample spacing of 200 nm, we map $B_z(x, y)$. We can also measure $B_{lever} \propto dB_z/dz$ by demodulating the SQUID-on-lever response at the cantilever oscillation frequency. Due to spectral filtering, the resulting signal contains less noise than DC measurements of B_z. The spatial resolution of the SSM is limited by the tip-sample spacing and by the 270-nm SQUID-on-lever effective diameter. Maps of $B_z(x, y)$ and $B_{lever}(x, y)$ are taken using a scanning probe microscopy controller (Specs) at a scan rate of 330 nm s^{-1}, 338 ms per pixel, and typically take several hours.

Micromagnetic simulations

We simulate the flake's magnetization configuration using the *Mumax³* software package[40,41]. The software utilizes the Landau-Lifshitz-Gilbert micromagnetic formalism with finite-difference discretization. To mimic the layered structure of CGT we make use of the finite difference mesh by setting the thickness of a mesh cell to the thickness of a CGT layer. The geometry, estimated from optical images, and corresponding number of layers, is reproduced for three different parts of the studied CGT flake. The structure is discretized into cells of size $3.5 \text{nm} \times 3.5 \text{ nm} \times 0.7 \text{ nm}$. The saturation magnetization is chosen to be $M_{sat} = 2.2 \, \mu_B$/Cr, based on the linear fit of the magnetization presented in Fig. 1f. In order to reproduce the observed presence of domains in the thicker and their absence in the thinner parts of the flake, we assume that the magnetocrystalline anisotropy K_u of the system is similar to its shape anisotropy K_s[42,43] which can be approximated from that of an infinitely extended plate: $K_s = 1/2 \, \mu_0 M_{sat}^2 \approx 13,600$ J m^{-3}[35]. The intra-layer exchange stiffness A_{ex} is estimated based on the Curie temperature T_c[1,44]. Both K_u and A_{ex} were further optimized from this starting point to match our both measured hysteresis curves and magnetic images. Two values were used for the $K_u = 13,700$ J m^{-3} for the simulation of the thicker part of the sample (11–15 layers) and $K_u = 12,800$ J m^{-3} for the thinner parts (3–9 layers). This change was implemented since domains start forming at different H_z for the thinner and thicker parts. The intra-layer exchange stiffness was also modulated for the three different simulated regions with $A_{ex} = 2.5 \cdot 10^{-13}$ J m^{-1}, $1.8 \cdot 10^{-13}$ J m^{-1} and $1.4 \cdot 10^{-13}$ J m^{-1} for the thicker (12–15 layers), intermediate (7–9 layers) and thinner (3–5 layers) regions, respectively. This was again done to match measured magnetic hysteresis and respective magnetic field maps. The interlayer exchange stiffness is assumed to be 3 % of the intralayer stiffness, estimated based on the ratio of the interlayer and intralayer exchange interactions between Cr atoms[45]. Small adjustments on the interlayer exchange stiffness do not change the magnetic behavior of the simulated flakes.

In order to generate simulated maps of $B_z(x, y)$ and $\frac{dB_z(x,y)}{dz}$, we use the magnetization maps generated by *Mumax³*. We calculate $B_z(x, y)$ at a height of 200 nm above the sample, corresponding to our SQUID-sample distance. $\frac{dB_z(x,y)}{dz}$ is calculated assuming $dz = 16$ nm, corresponding to the oscillation amplitude of the cantilever. Finally, we apply a Gaussian blurring of $2\sigma = 270$ nm to approximate the point-spread function of the SQUID sensor.

Data availability

References

1. Gong, C. et al. Discovery of intrinsic ferromagnetism in two-dimensional van der Waals crystals. *Nature* **546**, 265–269 (2017).
2. Huang, B. et al. Layer-dependent ferromagnetism in a van der Waals crystal down to the monolayer limit. *Nature* **546**, 270–273 (2017).
3. Huang, B. et al. Emergent phenomena and proximity effects in two-dimensional magnets and heterostructures. *Nat. Mater.* **19**, 1276–1289 (2020).
4. Niu, B. et al. Coexistence of magnetic orders in two-dimensional magnet CrI$_3$. *Nano Lett.* **20**, 553–558 (2020).
5. Liu, Y. et al. Thickness-dependent magnetic order in CrI$_3$ single crystals. *Sci. Rep.* **9**, 13599 (2019).
6. Thiel, L. et al. Probing magnetism in 2D materials at the nanoscale with single-spin microscopy. *Science* **364**, 973–976 (2019).
7. Xu, Y. et al. Coexisting ferromagnetic-antiferromagnetic state in twisted bilayer CrI$_3$. *Nat. Nanotechnol.* **17**, 143–147 (2022).
8. Tong, Q., Liu, F., Xiao, J. & Yao, W. Skyrmions in the Moiré of van der Waals 2D Magnets. *Nano Lett.* **18**, 7194–7199 (2018).
9. Song, T. et al. Direct visualization of magnetic domains and Moiré magnetism in twisted 2D magnets. *Science* **374**, 1140–1144 (2021).
10. Wang, Q. H. et al. The magnetic genome of two-dimensional van der Waals materials. *ACS Nano* **16**, 6960–7079 (2022).
11. Mogi, M. et al. Current-induced switching of proximity-induced ferromagnetic surface states in a topological insulator. *Nat. Commun.* **12**, 1404 (2021).
12. Khela, M. et al. Laser-induced topological spin switching in a 2D van der Waals magnet. *Nat. Commun.* **14**, 1378 (2023).
13. Ostwal, V., Shen, T. & Appenzeller, J. Efficient spin-orbit torque switching of the semiconducting Van Der Waals ferromagnet Cr$_2$Ge$_2$Te$_6$. *Adv. Mater.* **32**, 1906021 (2020).
14. Chen, L. et al. Anisotropic magnon damping by zero-temperature quantum fluctuations in ferromagnetic CrGeTe$_3$. *Nat. Commun.* **13**, 4037 (2022).
15. Verzhbitskiy, I. A. et al. Controlling the magnetic anisotropy in Cr$_2$Ge$_2$Te$_6$ by electrostatic gating. *Nat. Electron.* **3**, 460–465 (2020).
16. Zhuo, W. et al. Manipulating ferromagnetism in few-layered Cr$_2$Ge$_2$Te$_6$. *Adv. Mater.* **33**, 2008586 (2021).
17. O'Neill, A. et al. Enhanced room temperature ferromagnetism in highly strained 2D semiconductor Cr$_2$Ge$_2$Te$_6$. *ACS Nano* **17**, 735–742 (2023).
18. Šiškins, M. et al. Nanomechanical probing and strain tuning of the Curie temperature in suspended Cr$_2$Ge$_2$Te$_6$-based heterostructures. *npj 2D Mater. Appl.* **6**, 41 (2022).
19. Noah, A. et al. Interior and edge magnetization in thin exfoliated CrGeTe$_3$ films. *Nano Lett.* **22**, 3165–3172 (2022).
20. Lohmann, M. et al. Probing magnetism in insulating Cr$_2$Ge$_2$Te$_6$ by induced anomalous Hall effect in Pt. *Nano Lett.* **19**, 2397–2403 (2019).
21. Noah, A. et al. Nano-patterned magnetic edges in CrGeTe$_3$ for quasi 1-D spintronic devices. *ACS Appl. Nano Mater.* **6**, 8627–8634 (2023).
22. Gupta, V. et al. Manipulation of the van der Waals magnet Cr$_2$Ge$_2$Te$_6$ by spin-orbit torques. *Nano Lett.* **20**, 7482–7488 (2020).
23. Han, M.-G. et al. Topological magnetic-spin textures in two-dimensional van der Waals Cr$_2$Ge$_2$Te$_6$. *Nano Lett.* **19**, 7859–7865 (2019).
24. Wyss, M. et al. Magnetic, thermal, and topographic imaging with a nanometer-scale SQUID-On-lever scanning probe. *Phys. Rev. Appl.* **17**, 034002 (2022).

25. Broadway, D. et al. Improved current density and magnetization reconstruction through vector magnetic field measurements. *Phys. Rev. Appl.* **14**, 024076 (2020).

26. Suzuki, M. et al. Magnetic anisotropy of the van der Waals ferromagnet $Cr_2Ge_2Te_6$ studied by angular-dependent x-ray magnetic circular dichroism. *Phys. Rev. Res.* **4**, 013139 (2022).

27. Zhang, X. et al. Magnetic anisotropy of the single-crystalline ferromagnetic insulator $Cr_2Ge_2Te_6$. *Jpn. J. Appl. Phys.* **55**, 033001 (2016).

28. Ji, H. et al. A ferromagnetic insulating substrate for the epitaxial growth of topological insulators. *J. Appl. Phys.* **114**, 114907 (2013).

29. Soumyanarayanan, A. et al. Tunable room-temperature magnetic skyrmions in Ir/Fe/Co/Pt multilayers. *Nat. Mater.* **16**, 898–904 (2017).

30. Avakyants, A., Orlova, N., Timonina, A., Kolesnikov, N. & Deviatov, E. Evidence for surface spin structures from first order reversal curves in $Co_3Sn_2S_2$ and Fe_3GeTe_2 magnetic topological semimetals. *J. Magn. Magn. Mater.* **573**, 170668 (2023).

31. Brandão, J. et al. Observation of magnetic skyrmions in unpatterned symmetric multilayers at room temperature and zero magnetic field. *Sci. Rep.* **9**, 4144 (2019).

32. Ba, Y. et al. Electric-field control of skyrmions in multiferroic heterostructure via magnetoelectric coupling. *Nat. Commun.* **12**, 322 (2021).

33. Fang, Y., Wu, S., Zhu, Z.-Z. & Guo, G.-Y. Large magneto-optical effects and magnetic anisotropy energy in two-dimensional $Cr_2Ge_2Te_6$. *Phys. Rev. B* **98**, 125416 (2018).

34. Bogdanov, A. N. & Panagopoulos, C. Physical foundations and basic properties of magnetic skyrmions. *Nat. Rev. Phys.* **2**, 492–498 (2020).

35. Hubert, A. & Schäfer, R. *Magnetic Domains: The Analysis of Magnetic Microstructures* (Springer, 1998).

36. Nielsen, J. W. Magnetic bubble materials. *Annu. Rev. Mater. Sci.* **9**, 87–121 (1979).

37. Zhang, S., van der Laan, G., Wang, W., Haghighirad, A. & Hesjedal, T. Direct observation of twisted surface skyrmions in bulk crystals. *Phys. Rev. Lett.* **120**, 227202 (2018).

38. Yao, Y. et al. Chirality flips of skyrmion bubbles. *Nat. Commun.* **13**, 5991 (2022).

39. Castellanos-Gomez, A. et al. Deterministic transfer of two-dimensional materials by all-dry viscoelastic stamping. *2D Mater.* **1**, 011002 (2014).

40. Vansteenkiste, A. et al. The design and verification of MuMax3. *AIP Adv.* **4**, 107133 (2014).

41. Exl, L. et al. LaBonte's method revisited: an effective steepest descent method for micromagnetic energy minimization. *J. Appl. Phys.* **115**, 17D118 (2014).

42. Yu, X. et al. Magnetic stripes and skyrmions with helicity reversals. *Proc. Natl Acad. Sci.* **109**, 8856–8860 (2012).

43. Belliard, L. et al. Stripe domains morphology versus layers thickness in CoPt multilayers. *J. Appl. Phys.* **81**, 5315–5317 (1997).

44. Coey, J. M. D. *Magnetism and Magnetic Materials* 1 edn (Cambridge University Press, 2010).

45. Zhu, F. et al. Topological magnon insulators in two-dimensional van der Waals ferromagnets $CrSiTe_3$ and $CrGeTe_3$: toward intrinsic gap-tunability. *Sci. Adv.* **7**, eabi7532 (2021).

Author contributions
M.P., K.B., and A.V. conceived the project. M.D. and T.K.C. fabricated the sample. K.B., A.V., and D.J. performed the experiment. K.B., D.J., and A.V. analyzed the data. A.V. and B.G. performed the micromagnetic simulations. M.P. and K.B. wrote the manuscript with input from A.V. and D.J. D.C., P.B. D.C. initiated the collaboration and M.P. provided supervision. All authors discussed the results and commented on the manuscript.

Competing interests
The authors declare no competing interests.

Additional information
Supplementary information The online version contains supplementary material available at https://doi.org/10.1038/s43246-024-00477-5.

Correspondence and requests for materials should be addressed to Martino Poggio.

Peer review information *Communications Materials* thanks the anonymous reviewers for their contribution to the peer review of this work. Primary Handling Editor: Aldo Isidori. A peer review file is available.

Reprints and permissions information is available at http://www.nature.com/reprints

Publisher's note Springer Nature remains neutral with regard to jurisdictional claims in published maps and institutional affiliations.